Discovering the Gell-Mann–Okubo formula with Kolmogorov-Arnold networks*

Jian-Yao He (贺渐尧)[1†] Xun Chen (陈勋)[1,2‡] Xiao-Yan Zhu (朱小彦)[3§] Wen Luo (罗文)[1¶]

[1]School of Nuclear Science and Technology, University of South China, Hengyang 421001, China
[2]INFN – Istituto Nazionale di Fisica Nucleare – Sezione di Bari, Bari 70125, Italy
[3]School of Mathematics and Physics, University of South China, Hengyang 421200, China

Abstract: Uncovering physical laws from experimental data is a fundamental goal of theoretical physics. In this work, we apply the spline-based, interpretable Kolmogorov–Arnold Network (KAN) to investigate the algebraic structure underlying the baryon octet and decuplet mass spectra. Within a symbolic regression framework and without imposing theoretical priors, KAN recovers a symbolic representation equivalent to the classical Gell-Mann–Okubo mass relations, which can be transformed into the standard form through algebraic rearrangement. Compared with conventional fitting approaches, this method achieves comparable predictive accuracy while providing substantially improved interpretability and analytical transparency. Our results demonstrate the potential of KAN as a powerful tool for symbolic discovery in hadron physics and for bridging data-driven modeling with fundamental physical laws.

Keywords: Gell-Mann–Okubo formula, machine learning, Kolmogorov-Arnold Networks

DOI: 10.1088/1674-1137/ae8006 **CSTR:** 32044.14.ChinesePhysicsC.50103107

I. INTRODUCTION

Within the Standard Model, hadrons —composite particles composed of quarks bound by the strong interaction —are described by Quantum ChromoDynamics (QCD). As a non-Abelian gauge theory, QCD successfully accounts for phenomena such as color confinement and asymptotic freedom [1–9]. However, its non-perturbative regime, which dominates the hadron spectrum, remains analytically challenging. Nevertheless, the hadron mass spectrum exhibits patterns that reflect the underlying $SU(3)$ flavor symmetry [10–12]. In the 1960s, Gell-Mann and Ne'eman introduced the Eightfold Way classification, which organized the rapidly expanding set of experimentally discovered hadrons into octets and decuplets according to symmetry principles [10–12]. This framework indirectly led to the quark model, in which baryons and mesons are understood as three-quark states and quark–antiquark pairs, respectively. The first observation of the exotic candidate $X(3872)$ in 2003 challenged this simple three-quark picture. Since then, numerous exotic candidates have been reported at major high-energy accelerators [13–22], motivating efforts to develop more general mass formulas capable of describing these new states and predicting future ones. Within a single $SU(3)$ multiplet, small mass splittings arise from differences in the up, down, and strange quark masses. To quantify this effect, Gell-Mann and Okubo proposed the well-known GMO mass formula [12], which serves both as a valuable phenomenological tool and as a benchmark for testing flavor-symmetry-breaking effects.

In recent years, machine learning (ML) has advanced significantly across a wide range of disciplines. In physics, ML has been used to explore theoretical frameworks [23, 24] and to analyze high-energy phenomena [25–40]. Machine learning techniques enable the extraction of physical information from high-dimensional data [41–44], a task that is often difficult to accomplish using traditional methods. Neural networks, in particular, are effective at approximating nonlinear mappings and uncovering hidden patterns in both experimental and simulated data. In hadron and nuclear physics, neural net-

Received 18 February 2026; Accepted 22 June 2026; Accepted manuscript online 23 June 2026

* Supported by the National Natural Science Foundation of China (NSFC) (12405154) and the European Union – Next Generation EU through research grant (P2022Z4P4B), "SOPHYA - Sustainable Optimised PHYsics Algorithms: fundamental physics to build an advanced society", under the PRIN 2022 PNRR program of the Italian Ministero dell'Università e Ricerca (MUR)

† E-mail: yaoyaoerg5251@163.com
‡ E-mail: chenxun@usc.edu.cn
§ E-mail: xyzhu0128@163.com
¶ E-mail: wenluo-ok@163.com

works have been successfully employed to predict meson properties with spontaneously emerging symmetries [45], to extract the strong coupling constant across the full energy range [46], to determine QCD parameters in magnetized matter [47], and to predict nuclear masses with quantified uncertainties [48]. In addition, machine learning methods have been widely used in broader areas of physics, including studies of phase transitions and representation learning, further highlighting their capacity to capture fundamental patterns in physical systems [49–51]. Physics-informed neural networks (PINNs) [52–54] and their extensions embed physical constraints directly into the learning process, thereby bridging the gap between data-driven models and theoretical frameworks.

Among emerging neural network architectures, the Kolmogorov–Arnold Network (KAN) [55, 56] is notable for its interpretability and symbolic regression capabilities. Inspired by the Kolmogorov–Arnold representation theorem, KAN replaces the fixed weights of conventional neural networks with learnable univariate functions, enabling it to represent complex multivariate relationships in a form that is both flexible and analytically tractable. By expressing learned relations in explicit symbolic form, KAN addresses the black-box limitation of conventional neural networks and enables transparent physical interpretation. Unlike traditional neural networks [57], symbolic regression methods [58, 59], or genetic algorithms [60], KAN combines the expressive power of neural networks with the interpretability of symbolic regression while offering higher sample efficiency and improved integration of physical priors. Applications of KAN in physics are steadily expanding; for example, it has been used to model and compute the heavy-quark potential through holographic methods combined with lattice QCD data [61]. Such successes highlight KAN's considerable potential for addressing complex scientific problems [61–64].

In this study, we employ a KAN-based symbolic regression approach to analyze baryon mass data from $SU(3)$ octets and decuplets. Our objectives are: (i) to recover the Gell-Mann–Okubo (GMO) formula [10–12] using modern data-driven techniques; (ii) to assess its generalization capability across different $SU(3)$ multiplets; and (iii) to demonstrate how KAN can bridge machine learning and interpretable physics. Notably, we not only successfully reconstruct the classical GMO formula [10–12] but also recover underlying relationships among quantum numbers within the octet and decuplet, offering new perspectives on flavor-symmetry breaking.

II. FRAMEWORK

In this section, we introduce the detailed training procedure. The fundamental structure is presented below:

A. Input data

In this study, we use the baryon masses of the $SU(3)$ octet and decuplet as the primary input data. To address the limitations imposed by the extremely small sample size, we construct two complementary data-construction strategies to examine the behavior of the KAN model under both idealized and realistic conditions.

In the first stage, aimed at probing the intrinsic symbolic representation capability of KAN in the absence of experimental noise, we construct an augmented (replicated) dataset by replicating the PDG central mass values for each baryon 1000 times while keeping the corresponding quantum numbers (I, Y) unchanged. This procedure corresponds to an effective zero-variance (Dirac-delta-like) limit of the data distribution, in which each mass value is fixed at its central value. It does not introduce additional physical information but stabilizes the symbolic regression process under small-sample conditions.

In the second stage, to reflect realistic experimental uncertainties, we generate an additional dataset by sampling baryon masses from Gaussian distributions $\mathcal{N}(\mu,\sigma^2)$, where μ is the PDG central value and σ corresponds to the reported experimental uncertainty. This Gaussian-perturbed dataset is constructed specifically for the decuplet analysis to evaluate the robustness of the model. Under such noise, the KAN model remains able to recover the linear GMO mass relation and accurately predict the mass of the Ω^- baryon.

The mass values are taken from the Particle Data Group (PDG) in Table 1 [65]. These datasets preserve the underlying $SU(3)$ symmetry structure while providing stable and physically meaningful inputs for the KAN neural network [55, 56] to perform symbolic regression.

Table 1. Properties of baryon multiplets under $SU(3)$ flavor symmetry. The masses (in MeV) are isospin-averaged values from the PDG database [65], with uncertainties covering the full range of observed states within each multiplet. Decuplet states ($J^P = 3/2^+$) and octet states ($J^P = 1/2^+$) are distinguished by their spin-parity quantum numbers and quark compositions.

Name	Symbol	I	Y	Mass/MeV
Octet				
Nucleons	N	$\frac{1}{2}$	1	939 ± 1
Lambda baryons	Λ	0	0	1116 ± 1
Sigma baryons	Σ	1	0	1193 ± 4
Xi baryons	Ξ	$\frac{1}{2}$	-1	1318 ± 3
Decuplet				
Delta baryons	Δ	$\frac{3}{2}$	1	1232 ± 2
Sigma baryons	Σ^*	1	0	1385 ± 3
Xi baryons	Ξ^*	$\frac{1}{2}$	-1	1533 ± 2
Omega baryon	Ω	0	-2	1672 ± 1

Based on this dataset, we apply KAN for symbolic regression to explore the relationships between baryon masses and quantum numbers. In the decuplet analysis, we consider two complementary settings. First, using the PDG central mass values without additional perturbations, we perform a standard fit based on the linear GMO form to establish a reference description of the equal-spacing pattern.

Second, to evaluate the robustness of the model under realistic experimental conditions, we construct a Gaussian-perturbed dataset in which baryon masses are sampled according to the reported PDG uncertainties. KAN is then applied to this dataset for symbolic regression.

Under such noisy conditions, KAN extracts a simple linear relation between baryon masses and hypercharge, consistent with the expected equal-spacing behavior. Moreover, the learned relation enables an accurate prediction of the Ω^- baryon mass, even though it is not explicitly enforced in the fitting procedure.

These results indicate that the KAN model can recover the underlying GMO structure in both idealized and noise-perturbed settings, demonstrating its robustness and stability in the presence of experimental uncertainties. Building on this structure, we further perform symbolic regression to reconstruct the explicit functional form of the decuplet Gell-Mann–Okubo formula. This also provides a simple data-driven validation of the equal-spacing rule in the decuplet.

For the octet analysis, we adopt the same preprocessing and stratified sampling procedures as in the first stage for the decuplet baryons. KAN symbolic regression is then applied to investigate the dependence of baryon masses on hypercharge (Y) and isospin (I). The model extracts a compact and physically interpretable expression that captures the observed quadratic dependence on Y and I. This relation serves as the basis for reconstructing the complete Gell-Mann–Okubo formula through further symbolic regression.

The final symbolic expressions obtained for both the octet and decuplet exhibit high accuracy and good interpretability and remain consistent with theoretical expectations of $SU(3)$ flavor-symmetry breaking [10–12].

B. Model selection

To ensure that the symbolic regression model is both physically interpretable and capable of accurately capturing the $SU(3)$ baryon mass patterns, we implemented a systematic model-selection process.

Initially, a custom-parameterized KAN model was trained using the L-BFGS optimizer, with sparsity-promoting regularization explicitly incorporated into the objective function. In particular, two regularization terms (*lamb* and *lambda_entropy*) were introduced to penalize redundant functional components and reduce structural complexity. All training procedures were conducted under fixed random seeds to ensure reproducibility.

After each training stage, a deterministic pruning operation (model.prune) was applied. This built-in procedure removes branches with negligible contributions based on the learned functional weights, thereby simplifying the network by retaining only the dominant functional pathways. Importantly, no manually defined pruning thresholds were introduced in this work. Instead, sparsity is governed entirely by the regularization terms during training, making the pruning process fully data-driven and reproducible.

Following pruning, the reduced model was retrained using the same optimization and regularization settings to refine the remaining functional structure and mitigate any potential performance degradation. This alternating procedure of regularized training, pruning, and retraining was repeated iteratively until convergence, as indicated by stable loss values and evaluation metrics.

Through this pipeline, the model progressively prunes redundant components and converges to a compact symbolic representation. Although the pipeline is largely automated, limited manual intervention is applied when necessary, mainly for algebraic simplification and presentation. This hybrid approach enables systematic derivation of the results while enhancing both interpretability and methodological transparency.

Upon achieving satisfactory performance, symbolic regression [59] was applied. Constrained by the Physics Filter, the regression avoided overly complex functional forms and yielded a physically interpretable expression:

$$M = aY + b\left[I(I+1) - \frac{1}{4}Y^2\right] + c, \tag{1}$$

where a, b, and c are free parameters estimated from the data.

C. *SU*(3)-consistent generalization

We assess generalization with respect to $SU(3)$ multiplet consistency, considering both symbolic structure and representation-wide coverage. For the model, a nontrivial requirement is that all members of a given multiplet share a single invariant symbolic form. For example, the KAN-based regression of the Gell–Mann–Okubo relation for octet baryons retains a consistent functional structure across all multiplet members. For the data, the model must perform reliably for all baryons within a given $SU(3)$ representation.

D. Loss function

Model performance is evaluated using the mean squared error [66–71] (MSE), defined as

$$\mathrm{MSE} = \frac{1}{n}\sum_{i=1}^{n}(\hat{y}_i - y_i)^2. \tag{2}$$

This metric measures the average squared deviation between predicted and observed values. During training, numerical gradient descent with a specified learning rate minimizes the MSE, thereby optimizing model parameters for predictive accuracy. In symbolic regression [59], optimization extends beyond parameter fitting to include structural discovery. Thus, MSE quantifies prediction error and supports the joint evolution of model structure and parameter convergence.

E. Training progress of decuplet baryons

To investigate possible latent linear patterns among the $SU(3)$ decuplet baryons, we applied KAN-based symbolic regression to their experimentally measured masses. Rather than imposing a predefined functional form, the network searched for a simple mathematical expression consistent with the data and symmetry constraints. After training, the resulting symbolic form exhibited a clear linear dependence between baryon masses and their quantum numbers, consistent with the expected equal-spacing behavior within the decuplet.

This data-driven discovery not only reaffirms the validity of $SU(3)$ flavor symmetry but also demonstrates the ability of the KAN model to recover fundamental linear relations directly from empirical data without prior assumptions. The extracted formula provides a quantitative link between the group-theoretic structure of the decuplet and the experimentally observed mass spectrum.

Figure 1 illustrates the KAN neural network architecture used to investigate the linear relations in the decuplet, which consists of two hidden layers. As shown in Table 2, the final results were obtained after two rounds of training and pruning. Beyond these two iterations, further training produced no change in the loss function, indicating that the model had converged. The final formula obtained for decuplet baryons is:

$$Y_{10} = 2I_{10} - 2. \tag{3}$$

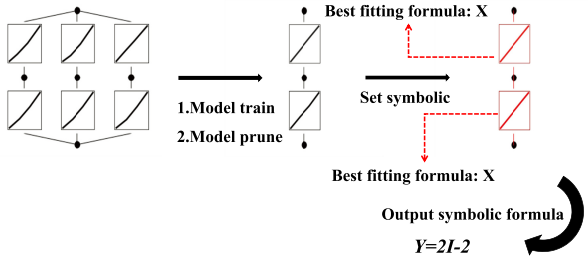

Fig. 1. (color online) Figure 1 illustrates the use of a KAN neural network to identify linear relationships among decuplet baryons.

Table 2. training log of decuplet linear.

Step	train loss	test loss
1	4.05×10^{-2}	4.29×10^{-2}
2	3.25×10^{-10}	1.73×10^{-10}

Building on the linear patterns identified within the $SU(3)$ decuplet, we performed symbolic regression to recover the explicit functional dependence of baryon masses on their quantum numbers. Using experimental data from the PDG [65], the KAN model was trained to learn this mapping in a data-driven yet physically constrained manner. The regression converged rapidly with low loss, indicating that the network effectively captured the underlying symmetry structure.

To obtain the GMO formula for the decuplet, we constructed a KAN with a (2,3,1) architecture, corresponding to the number of nodes in the input, hidden, and output layers, respectively, as shown in Fig. 2. The input variables are hypercharge Y and isospin I, and the output is the mass M. During training, the regularization parameters and learning rate were adaptively adjusted after each iteration to reduce the loss to an appropriate level. Simultaneously, the model automatically identified and removed redundant or ineffective branches, thereby improving generalization and reducing computational complexity. Through pruning, the network structure was simplified, retaining only the paths that contributed to the final symbolic regression. After ten training iterations, as shown in Table 3, the loss function showed no further change, indicating that the model had converged.

The analytical expression derived using symbolic regression is:

$$\begin{aligned} F(Y_{10}, I_{10}) = &-871.53(-0.1Y_{10} - 1)^2 + 0.05(Y_{10} + 1)^2 \\ &+ 22.04(-I_{10} - 0.24)^2 - 2.81(-0.7I_{10} - 1)^2 \\ &+ 2231.5. \end{aligned} \tag{4}$$

After expanding the expression and rounding each term to two decimal places, we obtain:

$$\begin{aligned} F(Y_{10}, I_{10}) = &-8.67Y_{10}^2 - 174.21Y_{10} + 20.66I_{10}^2 \\ &+ 6.65I_{10} + 1358.48. \end{aligned} \tag{5}$$

Based on the constraints of the GMO formula and the relation $Y_{10} = 2I_{10} - 2$, we simplify the expression step by step to approximate the target form:

$$\begin{aligned} F(Y_{10}, I_{10}) = &20.66I_{10}^2 + 20.66I_{10} - 14.01I_{10} \\ &- 8.67Y_{10}^2 - 174.21Y_{10} + 1358.48. \end{aligned} \tag{6}$$

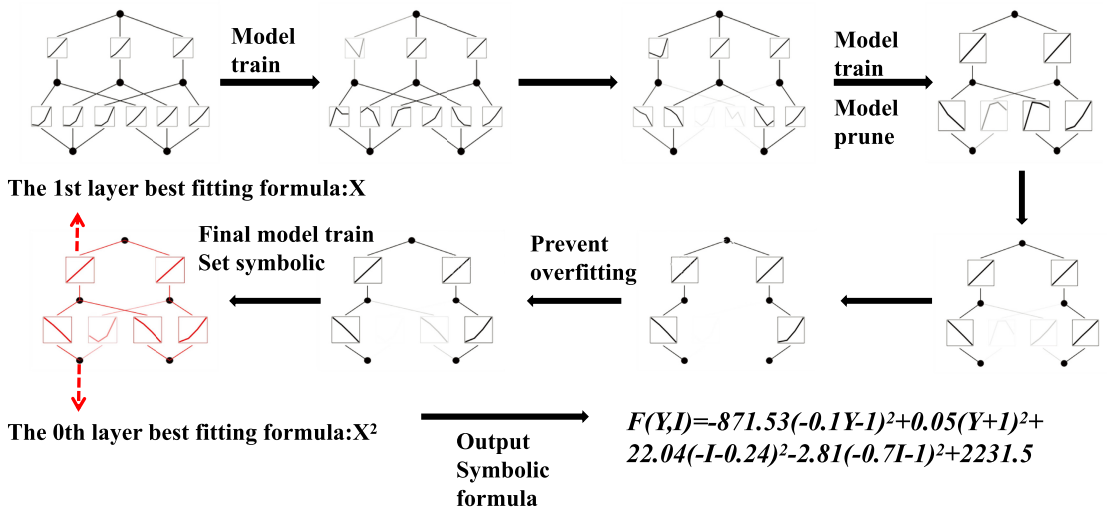

Fig. 2. (color online) Figure 2 illustrates the main workflow for using a KAN neural network to discover the Gell-Mann–Okubo formula for decuplet baryons, including the essential steps of model training, pruning, and symbolic regression.

Table 3. Training log of the decuplet GMO.

Step	train loss	test loss
1	1.11×10^{-3}	1.15×10^{-3}
2	1.30×10^{-3}	1.27×10^{-3}
3	1.51×10^{-3}	1.61×10^{-3}
4	1.65×10^{-2}	1.73×10^{-2}
5	2.52×10^{-2}	2.37×10^{-2}
6	7.60×10^{-4}	7.28×10^{-4}
7	5.02×10^{-4}	4.78×10^{-4}
8	4.37×10^{-3}	4.20×10^{-3}
9	4.02×10^{-4}	3.75×10^{-4}
10	9.90×10^{-4}	9.80×10^{-4}

Next, extract the common factor $Y_{10}(Y_{10}+1)$ from the terms involving Y_{10} and rewrite the remaining components:

$$F(Y_{10},I_{10}) = 20.66I_{10}(I_{10}+1) - 181.215Y_{10} - 8.67Y_{10}^2 + 1344.47. \quad (7)$$

To obtain a more compact expression, we rewrite the terms involving Y_{10} and $I_{10}(I_{10}+1)$ and replace $F(Y_{10},I_{10})$ with M_{10}. The final form is derived in Appendix A:

$$M_{10} = -90.51Y_{10}^2 - 672.27Y_{10} + 689.73 + 348.03I_{10}(I_{10}+1). \quad (8)$$

This result not only validates the physical interpretability of the KAN-based regression model but also highlights its potential as a tool for uncovering the underlying physical patterns encoded in the data.

The equal-spacing rule is a remarkably simple yet striking consequence of the GMO mass formula for the baryon decuplet. It states that, within the decuplet, each decrease by one unit in strangeness S (corresponding to the addition of a strange quark s) leads to an approximately constant increase in the baryon mass. This relation can be verified using experimental data:

1. The mass difference between Δ $(S=0)$ and Σ^* $(S=-1)$:

$$M(\Sigma^*) - M(\Delta) \approx 1385 - 1232 = 153\ \text{MeV}.$$

2. The mass difference between Σ^* $(S=-1)$ and Ξ^* $(S=-2)$:

$$M(\Xi^*) - M(\Sigma^*) \approx 1533 - 1385 = 148\ \text{MeV}.$$

3. The mass difference between Ξ^* $(S=-2)$ and Ω^- $(S=-3)$:

$$M(\Omega^-) - M(\Xi^*) \approx 1672 - 1533 = 139\ \text{MeV}.$$

These three mass differences are very similar, each approximately 140–150 MeV. This linear, equally spaced mass relationship is known as the equal spacing rule of the decuplet. Consequently, the GMO formula reduces to a linear relation,

$$M = M_0 + aY. \quad (9)$$

Here, M is the baryon mass, and M_0 and a are constants

parametrizing the $SU(3)$-symmetric contribution and its leading symmetry-breaking correction, respectively. Similarly, we use KAN to train on the data in Table 1 [65] and validate the equal-spacing rule [10–12] in the baryon decuplet. We perform symbolic regression directly on the data to test whether a linear relation between the baryon mass M and the hypercharge Y can be recovered.

As a reference, we first consider the noise-free setting using only the PDG central mass values. In this idealized case, the dataset is deterministic, and KAN successfully recovers the expected linear equal-spacing relation with very small training and test errors (on the order of 10^{-4}–10^{-3}). This result provides a baseline description of the decuplet structure.

The corresponding noise-free decuplet equal-spacing formula is:

$$M_{10} = 1382.16 - 146.71 Y_{10}. \tag{10}$$

We then consider a more realistic setting. To reflect experimental uncertainties, we construct an additional dataset by sampling decuplet baryon masses from Gaussian distributions centered on the PDG values, with standard deviations given by the reported experimental uncertainties. (The Ω^- baryon is excluded from the training set and used for validation.) This noise-perturbed dataset is used to evaluate the model's robustness. The increase in numerical loss compared with the noise-free case is expected, as the regression error reflects the variance of the introduced stochastic fluctuations.

The procedure follows the same overall training workflow, including iterative training, pruning, and symbolic regression, while the specific network architecture and training configurations are adjusted to better capture the linear structure of the decuplet equal-spacing relation. Multiple training rounds are performed to ensure stable convergence, as illustrated in Fig. 3 and Table 4.

Under these Gaussian fluctuations, KAN-based symbolic regression still extracts a stable linear relation

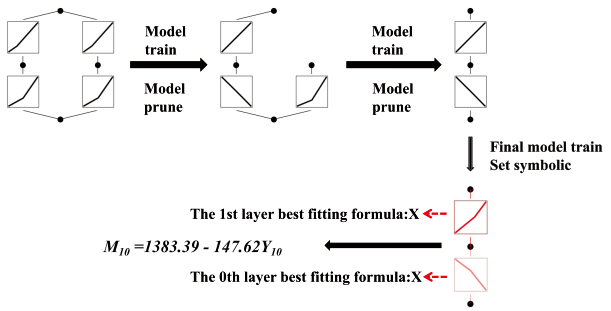

Fig. 3. (color online) Figure 3 illustrates the core process of using a KAN neural network to discover the equal-spacing rule in noise-perturbed decuplet baryons, including only the essential steps, such as training, pruning, and symbolic regression.

Table 4. Training log for the equal-spacing rule in the baryon decuplet.

Step	train loss	test loss
1	2.27	2.42
2	2.27	2.42

between baryon masses and hypercharge, consistent with the expected equal-spacing behavior of the decuplet. Moreover, the learned relation enables an accurate prediction of the Ω^- baryon mass, even though it is not explicitly enforced during training. These results demonstrate that the KAN framework maintains strong robustness and generalization capability under realistic noise conditions.

The corresponding quantitative evaluation, including RMSE, MSE, and R^2, further confirms the high quality of the symbolic regression. The resulting noisy decuplet equal-spacing formula is given by:

$$M_{10} = 1383.39 - 147.62 Y_{10}. \tag{11}$$

The calculated root mean square error (RMSE) is approximately 4.023, the mean square error (MSE) is approximately 16.181, and the coefficient of determination R^2 is approximately 0.9994.

Substituting these values into the decuplet equal-spacing formula gives the predicted mass of the Ω^- baryon:

$$M(\Omega^-) \approx 1678.63 \text{ MeV}.$$

Simultaneously, we observe the spontaneous emergence of a "dominant–correction" hierarchy. Through additive composition, the model effectively decouples the fitting task: smooth activation functions capture the leading-order physical dependence, whereas irregular functions serve as numerical residual compensators for local fluctuations. Although these perturbative terms lack intuitive symbolic forms, they are essential for maintaining high regression accuracy by offsetting small errors. This synergistic mechanism demonstrates KAN's ability to adaptively balance sparse physical representation and numerical precision.

F. Training progress of octet baryons

For the octet baryons, we analyzed the $SU(3)$ octet data using the same preprocessing and stratified sampling procedures as those used in the first stage for the decuplet baryons to uncover their hidden nonlinear interrelationships. Using the KAN symbolic regression workflow, we focused on the relationship between hypercharge Y and isospin I among the octet members. Figure 4 illustrates the KAN architecture employed for this task. This

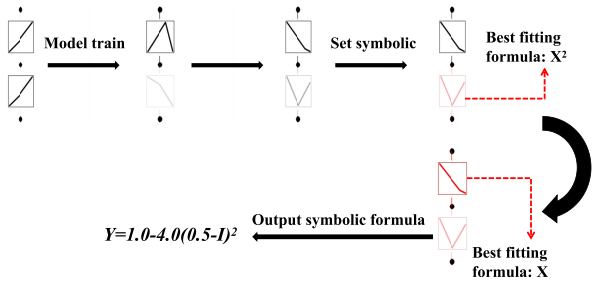

Fig. 4. (color online) Figure 4 illustrates the use of a KAN neural network to identify binary relationships among octet baryons.

Table 5. training log of octet binary.

Step	train loss	test loss
1	5.35×10^{-2}	5.35×10^{-2}
2	8.09×10^{-2}	8.04×10^{-2}
3	9.67×10^{-2}	1.02×10^{-1}
4	0.00	0.00

architecture is identical to that used to derive the linear relation for the decuplet, although the training procedure and function fitting differed. As shown in Table 5, the model converged after four training iterations. Finally, symbolic regression was applied to the model, yielding the relationship between Y and I.

$$Y_8^2 = 1.0 - 4.0(0.5 - I_8)^2. \tag{12}$$

We then employed KAN to identify the GMO formula for the octet. The initial neural network architecture was identical to that used for the decuplet, but the parameter adjustments during training differed from the previous setup. The detailed procedure is shown in Fig. 5. After eight training iterations, the loss function exhibited no further change; therefore, the model was considered to have converged, as summarized in Table 6. The figure retains only the key stages of training, such as pruning and optimization. Finally, symbolic regression was applied to the model, yielding the initial expression for the octet GMO formula:

$$F(Y_8, I_8) = 355.79(0.39 - I_8)^2 + 142.62(1 - 0.66Y_8)^2 + 918.77. \tag{13}$$

After splitting and retaining two decimal places, x_1 and x_2 are replaced with Y_8 and I_8, respectively. The initial expression is then obtained:

$$F(Y_8, I_8) = 62.13Y_8^2 + 355.79I_8^2 - 188.26Y_8 - 277.52I_8 + 1115.50. \tag{14}$$

To align the coefficients of I_8^2 and I_8, combine the expression above and temporarily substitute Y_8^2 for $0.25Y_8^2$ (*i.e.*, using the relation $0.25Y_8^2 = I_8 - I_8^2$). Details can be found in Appendix A.

The I_8-related terms can then be integrated into the original expression through the following transformation:

$$\begin{aligned} &39.135I_8 + 39.135I_8^2 - 39.135I_8 \\ &- 39.135I_8^2 - 277.52I_8 + 355.79I_8^2 \\ &= 39.135I_8(I_8 + 1) - 79.16375Y_8^2. \end{aligned} \tag{15}$$

Substituting the above result into the original expres-

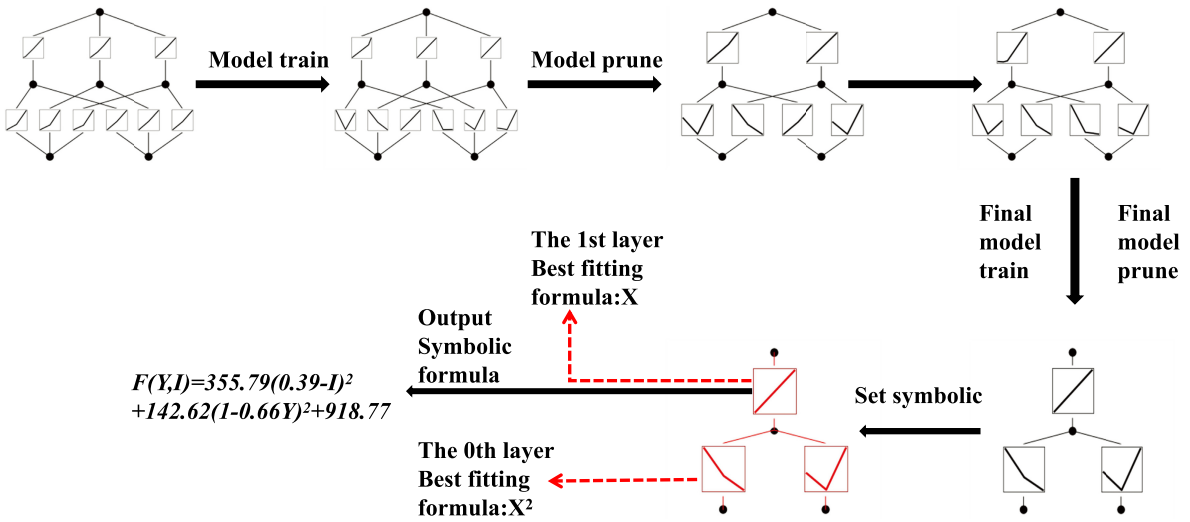

Fig. 5. (color online) Figure 5 illustrates the use of a KAN neural network to identify the Gell-Mann–Okubo formula for octet baryons.

Table 6. training log of octet GMO.

Step	train loss	test loss
1	1.27×10^{-2}	1.29×10^{-2}
2	4.60×10^{-3}	4.60×10^{-3}
3	7.87×10^{-4}	7.85×10^{-4}
4	8.79×10^{-3}	8.81×10^{-3}
5	4.04×10^{-3}	4.05×10^{-3}
6	3.64×10^{-9}	1.37×10^{-9}
7	5.19×10^{-8}	5.32×10^{-10}
8	2.92×10^{-11}	9.99×10^{-13}

sion, consolidating all coefficients, and replacing $F(Y_8, I_8)$ with M_8 yields the final form:

$$M_8 = -188.26Y_8 + 39.14I_8(I_8+1) - 17.03Y_8^2 + 1115.50. \tag{16}$$

G. Output

For the $SU(3)$ decuplet baryons (as shown in the decuplet section of Table 7), we analyze both central-value and noise-perturbed datasets. Using the PDG central mass values, the symbolic form corresponding to the GMO formula is successfully reproduced, and the linear equal-spacing relation for the decuplet is also recovered.

When Gaussian noise consistent with experimental uncertainties is introduced, KAN-based symbolic regression still extracts a stable linear relation between baryon masses and hypercharge, consistent with the GMO equal-spacing rule. Moreover, the learned relation enables accurate prediction of the Ω^- baryon mass, demonstrating the robustness of the model under realistic noise conditions.

For the $SU(3)$ octet baryons (as shown in the octet section of Table 7), the method reveals a multivariate correlation between Y and I. Substituting this relation into the symbolic GMO expression yields a compact and interpretable octet GMO formula that is consistent with the empirical mass hierarchy.

III. CONCLUSION AND OUTLOOK

In this work, we employ KAN to perform symbolic regression on experimental baryon mass data from $SU(3)$ octets and decuplets, with the dual aims of rediscovering the GMO mass formulas and refining their functional forms directly from data. Given the extremely limited sample size, we construct two complementary data-construction strategies while preserving the $SU(3)$ structure. In the first stage, an augmented dataset is formed by replicating the PDG central mass values while keeping the corresponding quantum numbers (e.g., isospin I and hypercharge Y) fixed. This stabilizes the symbolic-regression process without introducing additional physical information. In the second stage, to reflect realistic experimental conditions, an additional dataset is generated by sampling baryon masses from Gaussian distributions centered at the PDG values, with standard deviations given by the reported experimental uncertainties. The mass values are taken from the PDG and related literature [10–12, 72, 73]. Model performance, monitored via MSE, guides the tuning of regularization and learning-rate parameters. This is followed by pruning to remove redundant branches and retain only the paths relevant for symbolic extraction.

Table 7. The table presents all results for the decuplet and octet baryons obtained in this study using the KAN neural network.

Decuplet
Relation
$Y_{10} = 2I_{10} - 2$
$M_{10} = -90.51Y_{10}^2 - 672.27Y_{10} + 348.03I_{10}(I_{10}+1) + 689.73$
$M_{10}(equal-spacing) = 1383.39 - 147.62Y_{10}$
Octet
Relation
$Y_8^2 = 1.0 - 4.0(0.5 - I_8)^2$
$M_8 = -188.26Y_8 + 39.14I_8(I_8+1) - 17.03Y_8^2 + 1115.50$

Applying this workflow, KAN consistently extracts compact and physically interpretable symbolic expressions. For the octet, the model identifies a multivariate relation between Y and I, which serves as the basis for reconstructing the octet GMO formula and generalizes across N, Λ, Σ, and Ξ.

For the decuplet, we consider both idealized and noise-perturbed settings. Using the central-value dataset, the expected GMO formula is successfully recovered. When Gaussian noise consistent with experimental uncertainties is introduced, KAN is still able to extract a stable linear relation between baryon masses and hypercharge, consistent with the GMO equal-spacing rule. Moreover, the learned relation enables an accurate prediction of the Ω^- baryon mass, demonstrating the robustness of the approach under realistic noise conditions.

Beyond validating $SU(3)$ expectations, our results demonstrate the advantage of KAN as a data-driven, assumption-light method for rediscovering empirical mass formulas. The approach suggests several promising directions, including applying KAN to more intricate hadron spectra and exotic states [13, 74–78]. The present framework can be naturally extended to more complex hadron systems, particularly exotic hadrons, where different structural interpretations often coexist. A representative

example is the $\Lambda(1405)$ resonance, whose internal structure has long been debated in terms of conventional three-quark excitations, meson-baryon molecular components, dynamically generated states, and possible two-pole structures [79–81]. Recent studies have continued to investigate this state from different perspectives, including off-shell chiral dynamics, femtoscopic correlations, $SU(3)$ flavor filtering, production reactions, and lattice-QCD analyses [82–85].

From the perspective of interpretable machine learning, such systems provide natural testing grounds for extending the present KAN-based symbolic-regression framework beyond the reproduction of established mass relations. For exotic hadrons, different structural hypotheses—such as hadronic molecules, compact multiquark configurations, dynamically generated states, or mixed scenarios—can be encoded through distinct sets of physically motivated input variables, including threshold-related quantities, spin-coupling terms, flavor quantum numbers, channel-coupling information, pole positions, and reaction-dependent observables.

By applying KAN-based symbolic regression to these different feature representations, one can systematically compare the resulting expressions in terms of fitting accuracy, structural simplicity, parameter stability, and physical interpretability. Rather than directly determining the true underlying structure, this approach provides a transparent and unified framework for assessing which class of variables more naturally organizes the observed data. This is particularly relevant for exotic hadrons such as the $\Lambda(1405)$, where multiple competing interpretations exist and conventional model discrimination remains challenging.

This perspective highlights the broader methodological value of KAN in hadron physics, where competing physical pictures often coexist and data remain limited. Future extensions may integrate QCD inputs or expanded experimental datasets [72, 73, 86–102] to further refine symbolic forms and improve symbolic-regression pipelines, thereby enhancing interpretability and predictive power in high-energy physics. Overall, our findings highlight the potential of KAN to bridge data-driven modeling and interpretable physical laws.

Another promising application of the KAN framework lies in the analysis of Regge trajectories [78, 103–105] in hadron spectroscopy. Regge trajectories describe the empirical relation between the spin J and the squared mass M^2 of hadrons, which is approximately linear for many hadron families.

From a methodological perspective, this problem is well suited to KAN, as the goal is not only to fit the data but also to extract an interpretable functional relation between physical observables. By applying KAN-based symbolic regression to hadron spectrum data, one can directly learn the dependence of J on M^2 in a data-driven manner.

If the extracted relation is close to linear, this would provide an interpretable reconstruction of conventional Regge behavior. More importantly, potential deviations from strict linearity, if identified by the model, may encode physically relevant information, such as symmetry-breaking effects, family-dependent structures, or more complex internal hadron dynamics.

In this sense, KAN offers a complementary tool for Regge trajectory studies by providing not only numerical fits but also explicit functional forms that can be examined for physical interpretation.

Overall, the extracted symbolic expressions exhibit high accuracy and strong interpretability and remain consistent with theoretical expectations of $SU(3)$ flavor-symmetry breaking. Compared with purely numerical fitting approaches, the KAN framework provides an interpretable, data-driven pathway for uncovering analytic structures and relations among hadron multiplets.

More broadly, this study demonstrates that underlying symmetry patterns can be inferred from experimental data within an interpretable machine-learning framework. In particular, $SU(3)$ flavor symmetry and its symmetry-breaking structure are reflected in the extracted symbolic relations without explicitly imposing group-theoretical constraints, providing a model-independent and quantitative characterization of symmetry-breaking effects associated with quark mass differences.

Importantly, the present analysis highlights the capability of KAN in small-data regimes, where only a limited number of independent hadronic states are available. Although data augmentation is used to stabilize training, it does not introduce additional physical information, and the problem remains intrinsically small-sample. Under this constraint, the successful reconstruction of the GMO relation indicates that KAN can extract intrinsic functional dependencies from minimal data.

It should also be noted that the symbolic expressions obtained from KAN are not unique and are typically presented in expanded polynomial forms. Their transformation into conventional representations, such as expressions involving $I(I+1)$, involves only straightforward algebraic rearrangement without introducing additional physical assumptions. This suggests that KAN identifies the underlying functional structure, while the final compact form corresponds to a physically motivated choice of basis.

From this perspective, KAN provides a systematic and interpretable framework for uncovering functional relations in hadron mass spectra. Although the current dataset does not yet allow reliable extraction of higher-order corrections, the flexibility of the framework suggests strong potential for extension to more complex systems, where richer data may enable the identification of additional symmetry-breaking patterns in a data-driven and

physically interpretable manner.

Our implementation code has been uploaded to GitHub: https://github.com/yaoyaoer0406/yaoyaoer. We used version 1.0 of the KAN framework.

APPENDIX A: DERIVATION OF THE GMO RELATIONS FROM KAN OUTPUTS

A.1. Octet baryons

This Appendix provides detailed algebraic steps for transforming the raw symbolic expressions obtained by KAN into the standard GMO form. The following derivation involves only straightforward algebraic manipulations. The raw symbolic expression obtained from the KAN model for the baryon octet is:

$$M_8 = 355.79(0.39 - I_8)^2 + 142.62(1 - 0.66Y_8)^2 + 918.77. \tag{A1}$$

By expanding all terms and combining like terms while retaining two decimal places, we obtain:

$$M_8 = 62.13Y_8^2 + 355.79I_8^2 - 188.26Y_8 - 277.52I_8 + 1115.50. \tag{A2}$$

Using the implicit relation:

$$0.25Y_8^2 = I_8 - I_8^2, \tag{A3}$$

We aim to recover the standard $I(I+1)$ structure. To match the coefficients of I_8 and I_8^2, we compute:

$$\frac{355.79 - 277.52}{2} = 39.135. \tag{A4}$$

Rewriting the expression:

$$\begin{aligned} &39.135I_8 + 39.135I_8^2 - 39.135I_8 - 39.135I_8^2 \\ &\quad - 277.52I_8 + 355.79I_8^2 \end{aligned} \tag{A5}$$

$$= 39.135I_8(I_8+1) - 316.655I_8 + 316.655I_8^2 \tag{A6}$$

$$= 39.135I_8(I_8+1) - 316.655 \times 0.25Y_8^2 \tag{A7}$$

$$= 39.135I_8(I_8+1) - 79.16375Y_8^2. \tag{A8}$$

Substituting this result into the original expression, we obtain:

$$\begin{aligned} M_8 = {} & 39.135I_8(I_8+1) - 79.16375Y_8^2 - 188.26Y_8 \\ & + 62.13Y_8^2 + 1115.50. \end{aligned} \tag{A9}$$

After rounding to two decimal places:

$$M_8 = 39.14I_8(I_8+1) - 17.03Y_8^2 - 188.26Y_8 + 1115.50. \tag{A10}$$

A.2. Decuplet baryons

The raw symbolic expression obtained from the KAN model for the baryon decuplet is as follows (rounded to two decimal places):

$$\begin{aligned} M_{10} = {} & -871.53(-0.1Y_{10} - 1)^2 + 0.05(Y_{10} + 1)^2 \\ & + 22.04(-I_{10} - 0.24)^2 - 2.81(-0.7I_{10} - 1)^2 \\ & + 2231.5. \end{aligned} \tag{A11}$$

After expanding all terms and combining like terms, while retaining two decimal places, we obtain:

$$M_{10} = -8.67Y_{10}^2 - 174.21Y_{10} + 20.66I_{10}^2 + 6.65I_{10} + 1358.48. \tag{A12}$$

Using the implicit relation:

$$Y_{10} = 2I_{10} - 2. \tag{A13}$$

We again aim to recover the $I(I+1)$ structure. Rewriting:

$$\begin{aligned} M_{10} = {} & 20.66I_{10}^2 + 20.66I_{10} - 14.01I_{10} - 8.67Y_{10}^2 \\ & - 174.21Y_{10} + 1358.48. \end{aligned} \tag{A14}$$

To obtain a form consistent with the GMO structure, we further rewrite the expressions for Y_{10}^2 and $I_{10}(I_{10}+1)$. Using:

$$Y_{10}^2 = 4I_{10}^2 - 8I_{10} + 4. \tag{A15}$$

Using algebraic identities, we rewrite the expression in a basis consistent with the GMO structure:

$$\begin{aligned} M_{10} = {} & 20.66\,I_{10}(I_{10}+1) + 327.37\,I_{10}(I_{10}+1) \\ & - 327.37\,I_{10}(I_{10}+1) - 181.215\,Y_{10} \\ & - 8.67\,Y_{10}^2 + 1344.47 \end{aligned} \tag{A16}$$

$$=348.03\,I_{10}(I_{10}+1)-327.37\times\frac{Y_{10}^2+6Y_{10}+8}{4}$$
$$+1344.47-181.215\,Y_{10}-8.67\,Y_{10}^2. \quad \text{(A17)}$$

$$=-90.5125\,Y_{10}^2-672.27\,Y_{10}+348.03\,I_{10}(I_{10}+1)$$
$$+689.73. \quad \text{(A18)}$$

$$=-90.51\,Y_{10}^2-672.27\,Y_{10}+348.03\,I_{10}(I_{10}+1)$$
$$+689.73. \quad \text{(A19)}$$

APPENDIX B: COMPARISON OF KAN WITH OTHER MACHINE LEARNING METHODS

To further evaluate the performance of the KAN-based symbolic regression approach, we compare it with ordinary least squares (LS) and PySR, a genetic programming-based symbolic regression method, and discuss its differences from AI Feynman.

B.1. Comparison with least squares

We first compare the KAN method with the least squares (LS) approach in terms of parameter extraction accuracy and stability. For the baryon octet, we adopt the standard GMO functional form

$$M=aY+b\left[I(I+1)-\frac{1}{4}Y^2\right]+c, \quad \text{(B1)}$$

and perform an LS fit using the PDG central values.

The LS fit yields

$$M_8=-189.50\,Y+40.00\left[I(I+1)-\frac{1}{4}Y^2\right]+1111.50, \quad \text{(B2)}$$

with an MSE of 10.12, an RMSE of 3.18 MeV, an MAE of 2.99 MeV, and $R^2=0.99$.

In comparison, the KAN model learns a symbolic expression

$$M_8=-188.26Y+39.14I(I+1)-17.03Y^2+1115.50, \quad \text{(B3)}$$

with improved accuracy: MSE = 1.21, RMSE = 1.10 MeV, MAE = 0.94 MeV, and $R^2=0.99$. Figure B1 shows that both methods reproduce the octet masses with high precision, while Fig. B2 shows that KAN achieves better fitting accuracy.

To further evaluate robustness, we perform a noise-stability test by injecting Gaussian noise with a standard deviation of $\sigma=5$ MeV into the mass data. Multiple independent trials are conducted (50 for KAN and 500 for LS). To ensure a fair comparison, the symbolic form is fixed to be identical for both methods, such that only the parameter-extraction procedure differs.

We define stability as the dispersion of the extracted parameters (a,b,c) across these noisy realizations. As shown in Figs. B3, B4, and B5, the LS method is more sensitive to local noise fluctuations, resulting in larger variations in the fitted parameters. In contrast, KAN exhibits substantially improved stability, with the extracted

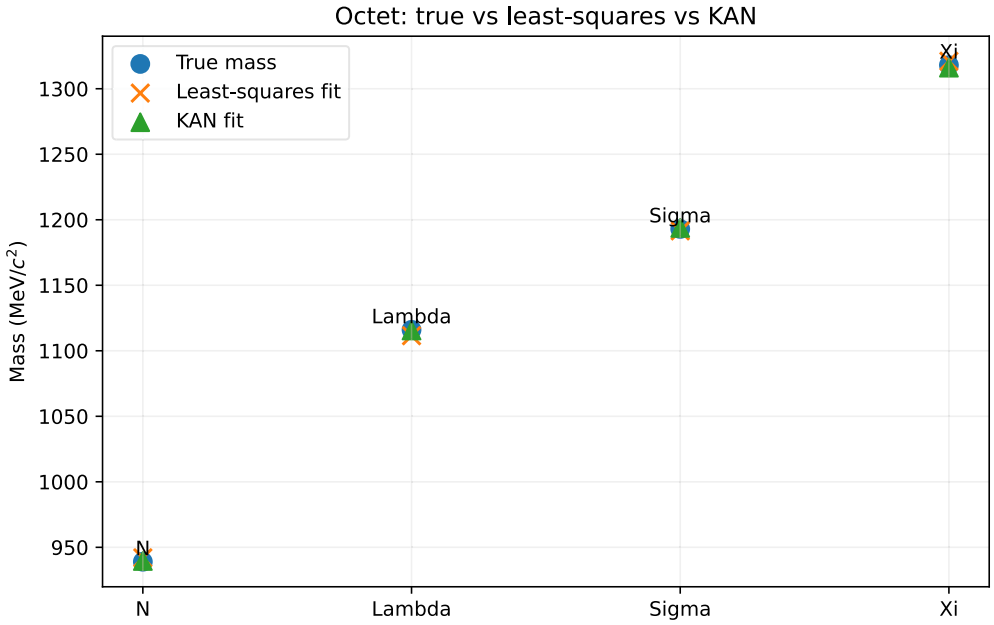

Fig. B1. (color online) As shown in Figure B1, both the least-squares method and KAN effectively fit the central values of the baryon octet, producing good results in both cases.

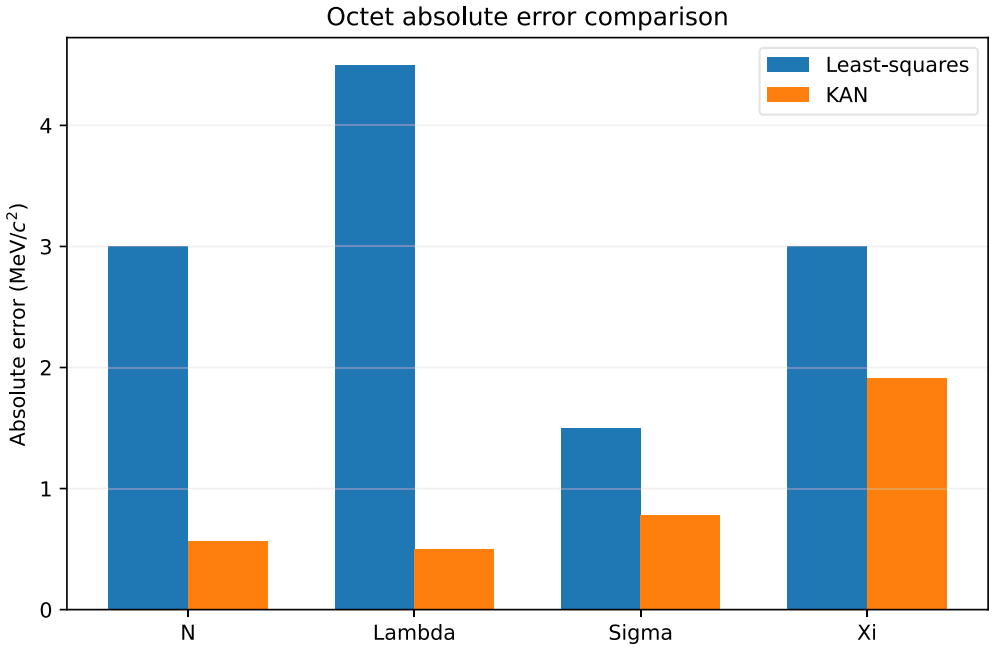

Fig. B2. (color online) As shown in Figure B2, KAN exhibits smaller absolute errors in fitting most octet baryons. This indicates that the results produced by KAN are more closely aligned with the central values of the baryon octet.

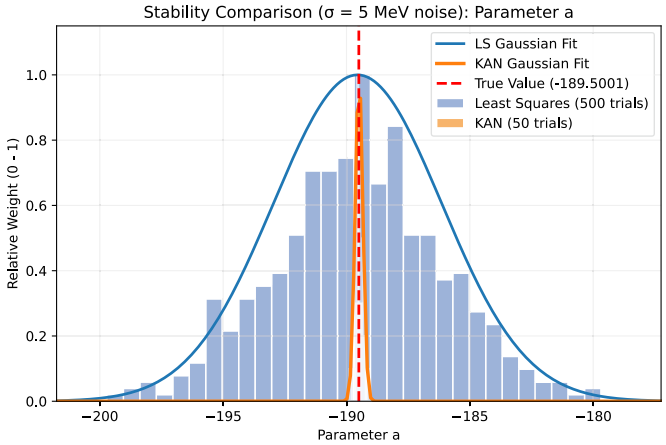

Fig. B3. (color online) Figure B3 compares the fitting stability of the two methods for parameter a under Gaussian noise with $\sigma = 5$ MeV. The figure shows that, at the same noise level, the KAN method yields a more stable, less biased, and narrower distribution of parameter a than traditional least-squares Gaussian fitting.

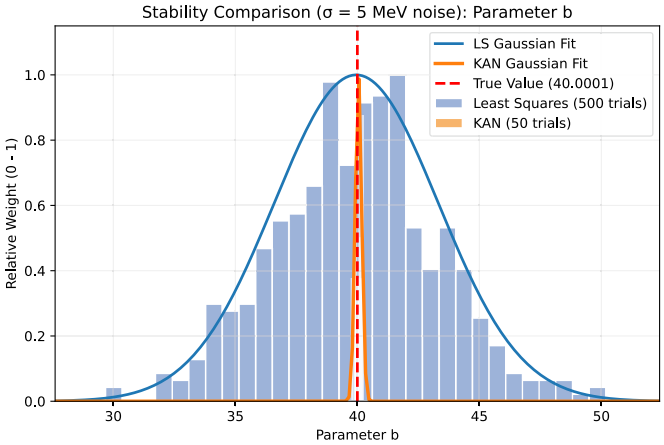

Fig. B4. (color online) Figure B4 compares the fitting stability of the two methods for parameter b under Gaussian noise with $\sigma = 5$ MeV. The figure shows that, at the same noise level, the KAN method yields a more stable, less biased, and narrower distribution of parameter b than traditional least-squares Gaussian fitting.

parameters forming a more concentrated distribution around the expected values.

This enhanced robustness can be attributed to two factors. First, the KAN training process incorporates intrinsic regularization, which suppresses overfitting to high-frequency noise. Second, KAN employs a two-stage extraction procedure: it first captures the global functional structure using B-spline representations and then, after fixing the symbolic form (via `fix_symbolic`), refines the parameters within a stable functional manifold.

Consequently, compared with the LS method, KAN yields parameter estimates with smaller variance under Gaussian perturbations, demonstrating superior robustness under noisy conditions.

B.2. Comparison with PySR

We further compare the KAN-based symbolic regression approach with PySR, a representative genetic programming-based method used in Ref. [101]. In that study, additional physics-inspired filtering rules were intro-

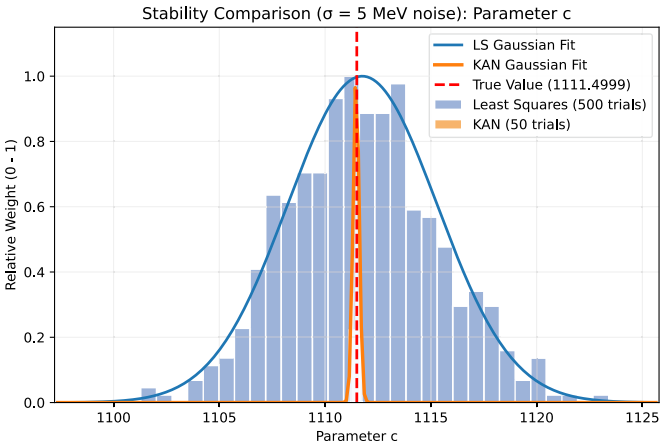

Fig. B5. (color online) Figure B5 compares the fitting stability of the two methods for parameter c under Gaussian noise with σ = 5 MeV. The figure shows that, at the same noise level, the KAN method yields a more stable, less biased, and sharper distribution of parameter c than traditional least-squares Gaussian fitting.

duced to guide the search toward physically meaningful expressions.

We emphasize that no additional physics-inspired filtering or feature engineering is applied to PySR in this comparison, allowing us to assess its baseline performance under minimal prior assumptions.

Using only the central values of the baryon octet, KAN recovers a compact and physically interpretable expression with RMSE = 1.10 MeV. In comparison, PySR, using only the basic input variables (I, Y), produces the empirical expression

$$M_8 = 79.999 I_8^2 - 189.50 Y_8 + 1111.50, \tag{B4}$$

with RMSE = 3.18 MeV. Although this expression provides a reasonable numerical fit, it does not reproduce the canonical GMO structure.

We further consider a guided PySR setup by including additional features (I^2, Y^2, $I(I+1)$). In this case, the fitting accuracy improves (RMSE = 0.75 MeV); however, the resulting expressions become more complex and involve higher-order mixed terms, which deviate from the expected GMO functional form and reduce interpretability.

In addition, in our sample-efficiency test, PySR fails to recover GMO-like expressions across all tested octet subsets, whereas KAN consistently extracts compact and physically meaningful symbolic relations.

The quantitative comparison of recovered expressions and fitting accuracy is summarized in Table B1, while the comparison of model characteristics is given in Table B2. These results indicate that, under the same data and input conditions, KAN provides a better balance between fitting accuracy, structural simplicity, and physical interpretability.

Table B1. Recovered expressions and fitting accuracy.

Method	Input features	Recovered expression
KAN	I, Y	$-188.26Y + 39.14I(I+1)$ $-17.03Y^2 + 1115.50$
PySR raw	I, Y	$79.999245I^2 - 189.49992Y$ $+1111.5004$
PySR guided	$I, Y, I^2, Y^2, I(I+1)$	$-3.1943I^3Y + 19.0113I^3$ $-187.7033Y + 1117.1418$

Note: RMSE(KAN) = 1.1006 MeV, RMSE(PySR raw) = 3.1820 MeV, RMSE(PySR guided) = 0.7452 MeV.

Table B2. Model characteristics comparison.

Method	Complexity	GMO-like	Interpretability
KAN	8	Yes	High
PySR raw	5	No	Medium
PySR guided	9	No	Low

Note: Generally speaking, the symbolic complexity of an expression is determined collectively by the number of operational nodes, the number of terms, and the presence of nonlinear structures. This definition follows common practice in symbolic regression, where expression complexity is used as a proxy for interpretability.

References

[1] D. J. Gross and F. Wilczek, Phys. Rev. Lett. **30**, 1343 (1973)
[2] H. D. Politzer, Phys. Rev. Lett. **30**, 1346 (1973)
[3] C. G. Callan Jr, Phys. Rev. D **2**, 1541 (1970)
[4] K. Symanzik, Commun.Math. Phys. **18**, 227 (1970)
[5] V. Vanyashin and M. Terent'ev, Sov. Phys. JETP **21**, 375 (1965)
[6] I. Khriplovich, *GREEN'S FUNCTIONS IN THEORIES WITH NON-ABELIAN GAUGE GROUP*, Tech. Rep. (Inst. of Nuclear Physics, Novosibirsk, USSR, 1969)
[7] H. Fritzsch, M. Gell-Mann, and H. Leutwyler, Phys. Lett. B **47**, 365 (1973)
[8] D. J. Gross and F. Wilczek, Phys. Rev. D **8**, 3633 (1973)
[9] H. D. Politzer, Phys. Rep. **14**, 129 (1974)
[10] M. Gell-Mann, *The eightfold way: A theory of strong interaction symmetry*, The Eightfold Way (CRC Press, 2018), p. 11
[11] S. Okubo, Prog. Theor. Phys. **27**, 949 (1962)
[12] M. Gell-Mann, *Symmetries of baryons and mesons*, The eightfold way (CRC Press, 2018), p. 216
[13] H. X. Chen, W. Chen, X. Liu *et al.*, Phys. Rep. **639**, 1 (2016)
[14] Y. R. Liu, H. X. Chen, W. Chen *et al.*, Prog. Part. and Nucl. Phys. **107**, 237 (2019)

[15] H. X. Chen, W. Chen, X. Liu *et al.*, Rep. Prog. Phys. **80**, 076201 (2017)
[16] Y. Dong, A. Faessler, and V. E. Lyubovitskij, Prog. Part. and Nucl. Phys. **94**, 282 (2017)
[17] R. F. Lebed, R. E. Mitchell, and E. S. Swanson, Prog. Part. and Nucl. Phys. **93**, 143 (2017)
[18] F. K. Guo, C. Hanhart, U. G. Meißner *et al.*, Rev. Mod. Phys. **90**, 015004 (2018)
[19] R. M. Albuquerque, J. M. Dias, K. Khemchandani *et al.*, J. Phys. G: Nucl. Part. Phys. **46**, 093002 (2019)
[20] Y. Yamaguchi, A. Hosaka, S. Takeuchi *et al.*, J. Phys. G: Nucl. Part. Phys. **47**, 053001 (2020)
[21] F. K. Guo, X. H. Liu, and S. Sakai, Prog. Part. and Nucl. Phys. **112**, 103757 (2020)
[22] N. Brambilla, S. Eidelman, C. Hanhart *et al.*, Phys. Rep. **873**, 1 (2020)
[23] S. J. Wetzel, R. G. Melko, J. Scott *et al.*, Phys. Rev. Res. **2**, 033499 (2020)
[24] M. Song, M. S. Oh, Y. Ahn *et al.*, Chin. Phys. C **45**, 073111 (2021)
[25] Y. D. Hezaveh, L. P. Levasseur, and P. J. Marshall, Nature **548**, 555 (2017)
[26] S. Soma, L. Wang, S. Shi *et al.*, Phys. Rev. D **107**, 083028 (2023)
[27] L. G. Pang, K. Zhou, N. Su *et al.*, Nature Commun. **9**, 210 (2018)
[28] X. Chen and M. Huang, Phys. Rev. D **109**, L051902 (2024)
[29] A. Radovic, M. Williams, D. Rousseau *et al.*, Nature **560**, 41 (2018)
[30] D. Guest, K. Cranmer, and D. Whiteson, Annu. Rev. Nucl. Part. Sci. **68**, 161 (2018)
[31] K. Albertsson, P. Altoe, D. Anderson *et al.*, *Machine learning in high energy physics community white paper*, Journal of Physics: Conference Series, Vol. 1085 (IOP Publishing, 2018), p. 022008
[32] J. Kim, G. Pederiva, and A. Shindler, Phys. Lett. B **856**, 138894 (2024)
[33] K. Zhou, L. Wang, L. G. Pang *et al.*, Prog. Part. and Nucl. Phys. **135**, 104084 (2024)
[34] G. Aarts, K. Fukushima, T. Hatsuda *et al.*, Nature Rev. Phys. **7**, 154 (2025)
[35] L. Jiang, L. Wang, and K. Zhou, Phys. Rev. D **103**, 116023 (2021)
[36] X. Chen and M. Huang, JHEP **2025**(02), 123 (2025)
[37] M. Mansouri, K. Bitaghsir Fadafan, and X. Chen, Eur. Phys. J. C **86**, 321 (2026)
[38] W. C. Dai, O. Y. Luo, B. Chen *et al.*, Phys. Lett. B **877**, 140511 (2026)
[39] J. Mei, L. Wang, and M. Huang, (2025), arXiv: 2507.22012
[40] P. Xiang, Y. S. Zhao, and X. G. Huang, Chin. Phys. C **46**, 074110 (2022)
[41] X. K. Du, P. Guo, X. H. Wu *et al.*, Chin. Phys. C **47**, 074108 (2023)
[42] Y. Wu, L. Xiao, and Y. Zhang, Chin. Phys. C **50**, 033105 (2026)
[43] J. Li and H. Sun, Chin. Phys. C **49**, 093106 (2025)
[44] Y. Wu, K. Wang, C. Li *et al.*, Chin. Phys. C **49**, 013110 (2025)
[45] X. Tong, W. Feng, W. Xu *et al.*, Chin. Phys. Lett. **43**, 020201 (2026)
[46] X. Y. Wang, C. Dong, and X. Liu, Chin. Phys. Lett. **41**, 031201 (2024)
[47] Z. Ding, F. Lin, and X. Wang, (2026), arXiv: 2603.29269
[48] S. Qu, J. Y. Zhang, and M. Bao, Chin.. Phys. C **49**, 104106 (2025)
[49] S. C. Bai and S. J. Ran, Chin. Phys. Lett. **41**, 120701 (2024)
[50] Y. G. Ma, L. G. Pang, R. Wang *et al.*, Chin. Phys. Lett. **40**, 122101 (2023)
[51] X. Li, R. Guo, Y. Zhou *et al.*, Chin. Phys. C **47**, 034101 (2023)
[52] M. Raissi, P. Perdikaris, and G. E. Karniadakis, J. Comput. Phys. **378**, 686 (2019)
[53] P. H. Chiu, J. C. Wong, C. Ooi *et al.*, Comput. Methods Appl. Mech. Eng. **395**, 114909 (2022)
[54] P. Wen, C. Lin, L. Yang *et al.*, Chin. Phys. C **49**, 084109 (2025)
[55] Z. Liu, Y. Wang, S. Vaidya *et al.*, Kan: Kolmogorov–arnold networks, *International conference on learning representations* (2025)
[56] Z. Liu, P. Ma, Y. Wang *et al.*, Phys. Rev. X **15**, 041051 (2025)
[57] Z. Liu and M. Tegmark, Phys. Rev. Lett. **126**, 180604 (2021)
[58] S.-M. Udrescu and M. Tegmark, Science Advances **6**, eaay2631 (2020)
[59] M. Schmidt and H. Lipson, Science **324**, 81 (2009)
[60] Z. Zhang, R. Ma, J. Hu *et al.*, Chin. Phys. Lett. **39**, 111201 (2022)
[61] O. Y. Luo, X. Chen, F. P. Li *et al.*, Eur. Phys. J. C **85**, 637 (2025)
[62] N. R. Panczyk, O. F. Erdem, and M. I. Radaideh, Energy and AI **22**, 100595 (2025)
[63] C. Guo, L. Sun, S. Li *et al.*, Physics of Fluids **37**, 095120 (2025)
[64] H. Hao, X. Zhang, B. Li *et al.*, (2024), arXiv: 2405.16494
[65] K. Nakamura, J. Phys. G: Nucl. Part. Phys. **37**, 075021 (2010)
[66] T. Hastie, R. Tibshirani, J. Friedman *et al.*, *The elements of statistical learning*, (2009)
[67] C. M. Bishop, *Pattern recognition and machine learning by Christopher M. Bishop*, Vol. 400 (Springer Science+ Business Media, LLC Berlin, Germany: 2006)
[68] I. Goodfellow, Y. Bengio, and A. Courville, *Deep learning* (MIT press Cambridge, 2016)
[69] S. Geman, E. Bienenstock, and R. Doursat, Neural Computation **4**, 1 (1992)
[70] K. P. Murphy, *Machine learning: a probabilistic perspective* (MIT press, 2012)
[71] T. Hastie, R. Tibshirani, and J. Friedman, *An introduction to statistical learning*, (2009), course notes
[72] Y. F. Liu, W. J. Xing, X. Y. Wu *et al.*, Phys. Rev. C **105**, 044904 (2022)
[73] S. Katel, H. Li, Z. Zhao *et al.*, (2024), arXiv: 2412.05333
[74] H. Garcilazo and A. Valcarce, Symmetry **17**, 1324 (2025)
[75] T. Hyodo, (2025), arXiv: 2503.15376
[76] G. Yang, J. Ping, and J. Segovia, Symmetry **12**, 1869 (2020)
[77] W. T. Lyu, L. J. Liu, and E. Wang, Eur. Phys. J. C **85**, 503 (2025)
[78] P. D. Collins and E. J. Squires, *Regge poles in particle physics*, Vol. 45 (Springer, 2006)
[79] D. Jido, J. Oller, E. Oset *et al.*, Nucl. Phys. A **725**, 181 (2003)

[80] T. Hyodo and D. Jido, Prog. Part. and Nucl. Phys. **67**, 55 (2012)
[81] J. Bulava, B. Cid-Mora, A. D. Hanlon *et al*, Phys. Rev. Lett. **132**, 051901 (2024)
[82] J. M. Xie, Z. W. Liu, J. X. Lu *et al*., (2026), arXiv: 2604.00791
[83] Y. B. He, X. H. Liu, L. S. Geng *et al*., Phys. Rev. D **113**, L051501 (2026)
[84] Y. Gao, X. Y. Wang, and X. Liu, (2026), arXiv: 2602.11480[nucl-th]
[85] J. S. Sucunza, T. Luu, and C. Urbach, *The Lambda 1405 at the $SU(3)$ point in lattice QCD*, Proceedings of the 42nd International Symposium on Lattice Field Theory (LATTICE2025), PoS, Vol. LATTICE2025 (Mumbai, India, 2025) p. 092, arXiv: 2602.19928[hep-lat]
[86] K. G. Wilson, Phys. Rev. D **10**, 2445 (1974)
[87] S. Durr, Z. Fodor, J. Frison *et al*., Science **322**, 1224 (2008)
[88] Y. Aoki, T. Blum, G. Colangelo *et al*., Eur. Phys. J. C **82**, 869 (2022)
[89] A. Bazavov, T. Bhattacharya, C. DeTar *et al*., Phys. Rev. D **90**, 094503 (2014)
[90] S. He, L. Li, Z. Li *et al*., Mechanics & Astronomy **67**, 240411 (2024)
[91] L. Zhang and M. Huang, Phys. Rev. D **106**, 096028 (2022)
[92] Y. Chen, D. Li, and M. Huang, Commun. Theor. Phys. **74**, 097201 (2022)
[93] R. Li, S. Han, Z. Lin *et al*., Phys. Rev. D **111**, 074026 (2025)
[94] K. Zhou, G. Endrődi, L. G. Pang *et al*., Phys. Rev. D **100**, 011501 (2019)
[95] X. Chen, D. Li, and M. Huang, Chin. Phys. C **43**, 023105 (2019)
[96] X. Chen, L. Zhang, D. Li *et al*., JHEP **03**, 073 (2021)
[97] X. Chen, D. Li, D. Hou *et al*., JHEP **2021**, 132 (2021)
[98] L. Zhu, X. Chen, K. Zhou *et al*., Phys. Rev. D **112**, 026019 (2025)
[99] W. J. Xing, S. Cao, G. Y. Qin *et al*., Phys. Rev. Lett. **134**, 052301 (2025)
[100] S. Cao and X. N. Wang, Rep. Prog. Phys. **84**, 024301 (2021)
[101] W. Zhang, Z. Zhang, J. Hu *et al*., Chin. Phys. Lett. **42**, 070202 (2025)
[102] H. A. Zeng, L. Wang, and M. Huang, (2025), arXiv: 2512.06044[hep-lat]
[103] D. Winney and A. P. Szczepaniak, (2025), arXiv: 2512.21805
[104] A. Inopin and G. Sharov, Phys. Rev. D **63**, 054023 (2001)
[105] J. K. Chen, Eur. Phys. J. C **84**, 356 (2024)